AIP Publishing Applied Physics Reviews ACCEPTED MANUSCRIPT
This is the author's peer reviewed, accepted manuscript. However, the online version of record will be different from this version once it has been copyedited and typeset.
PLEASE CITE THIS ARTICLE AS DOI: 10.1063/5.0335616

Exploration of enhanced stabilized-multibound-state-assisted optical response in symmetric dielectric metasurfaces

Kang Weng,[1,+] Wanting Wu,[2] Haodong Qian,[1] Zheng-Da Hu,[1] Weiying Qian,[1] Jicheng Wang,[1*] Yuting Yang,[2*] Mengze Li,[3] Sergei Khakhomov,[4] Feng Zhang[5*]

[1] *School of Optoelectronic Information and Physical Science, Jiangsu Provincial Research Center of Light Industrial Optoelectronic Engineering and Technology, Jiangnan University, Wuxi 214122, China*

[2] *School of Materials Science and Physics, China University of Mining and Technology, Xuzhou 221116, China*

[3] *School of Integrated Circuits, Nanjing University of Science and Technology, Nanjing 210094, China*

[4] *Departments of Optics and General Physics, Francisk Skorina Gomel State University, Gomel 246019, Belarus*

[5] *Department of Physics, Xiamen University, Xiamen, 361005, PR China*

** jcwang@jiangnan.edu.cn, yangyt@cumt.edu.cn, fzhang@xmu.edu.cn*

Abstract: Bound states in the continuum (BICs) exhibit enormous potential for advancing optical response due to their ultra-high Q factors. However, their practical applications are hindered by scattering losses caused by fabrication defects. This study proposes a strategy of merging multiple bound states at the Γ point of symmetric dielectric metasurfaces, aiming to enhance their optical response performance. Based on photonic crystal slabs with C_{4v}/C_{6v} symmetry, we designed structures that support symmetry-protected BICs and multiple accidental BICs capable of merging and separating. The Q factor of the $C4_v$ structure at the high-symmetry point remains consistently at 10^8. Then we can enhance the Q factor of the $C6_v$ structure up to 10^{10} by merging multiple accidental BICs. The merged states maintain excellent stability against variations in the lattice period, which significantly improves the optical responses. We experimentally achieved precise determination of the Q factor, and the results are in excellent agreement with the simulation data. This study of merged BICs provides a novel approach for the development of high-performance sensing and high-precision detection technologies.

Keywords: bound states in the continuum; metasurfaces; high-Q optical resonance

1. Introduction

Bound states in the continuum (BICs), characterized by theoretically infinite quality factors (Q factors), have revolutionized photonics by enabling unprecedented light confinement in open systems.[1-4] Despite residing within the radiative continuum, BICs are completely decoupled from far-field radiation, and can be categorized into two types based on their decoupling mechanisms. The first type originates from destructive interference: either destructive interference between different electromagnetic modes in the structure or between different waves of the same electromagnetic mode, thereby achieving decoupling from far-field radiation. Periodic geometric structures give rise to photonic band structures, analogous to the way periodic potentials generate electronic band structures in crystalline materials. Periodic slabs support guided resonances whose frequencies lie within the continuum of free-space radiative modes; these resonances typically exhibit finite lifetimes due to coupling to those modes. Although inherently radiative, destructive interference of far-field radiation induced by coupling between different resonant modes can also

AIP Publishing Applied Physics Reviews ACCEPTED MANUSCRIPT
This is the author's peer reviewed, accepted manuscript. However, the online version of record will be different from this version once it has been copyedited and typeset.
PLEASE CITE THIS ARTICLE AS DOI: 10.1063/5.0335616

form BICs. Resonance-coupled BICs in metasurfaces are further classified into Fabry-Pérot BICs and Friedrich-Wintgen BICs. Fabry-Pérot BICs are formed by constructing a pair of mirrors from two identical high-reflectivity periodic structures with a single radiative channel via guided resonance effects.[5-7] By adjusting the resonant frequency or spacing between the two structures such that the total phase shift of electromagnetic waves traveling back and forth equals an integer multiple of 2π, standing waves are established within the resulting Fabry-Pérot cavity, enabling electromagnetic wave trapping. When the distance between the two periodic structures supporting Fabry-Pérot BICs is reduced to zero (effectively forming a single periodic structure), destructive interference between radiations from two resonances co-located can also form BICs, known as Friedrich–Wintgen BICs.[8] The second type of BIC arises from structural symmetry mismatch. Microstructures with specific symmetries can confine even-symmetric resonant modes in the radiative continuum; these even-symmetric resonant modes are completely orthogonal to odd-symmetric radiative modes, leading to decoupling from far-field radiation and thereby forming BICs. This category is referred to as symmetry-protected BICs (SP-BICs).[9-11] As ideal BICs, SP-BICs exhibit the core characteristics of zero radiative energy leakage and zero linewidth, which renders them directly unobservable in spectroscopic measurements.[12] For practical engineering applications, symmetry-breaking modulation methods such as fabricating eccentric hole structures,[13] implementing splits,[14] or inducing structural tilting[15] are typically introduced to break the original symmetry of the system. Such symmetry breaking enables coupling between SP-BICs and the radiative continuum, forming effective radiative channels and ultimately converting SP-BICs into quasi-BICs (qBICs).[16-21] Notably, qBICs can be directly excited by external light sources without relying on specialized coupling structures or mechanisms, significantly lowering the application threshold. To date, qBIC-related mechanisms have been implemented in various photonic functional devices, including filters,[22] lasers,[23] nonlinear optical devices,[24] and optical sensors.[25-26]

Optical response refers to a controllable variation phenomenon of the optical properties (such as refractive index, absorption rate, scattering intensity and resonant frequency, etc.) of materials or structures in response to changes in the external environment under light-field illumination. This response has significant advantages including high sensitivity, rapid response, and non-contact detection capability. Particularly, it exhibits unique value in identifying subtle environmental disturbances and serves as the core foundation for constructing high-performance sensing systems. Benefiting from the core advantages of optical response, optical biosensors have become a research hotspot in the sensing field and attracted widespread attention. Over the past decade, remarkable breakthroughs have been achieved in the integrated research of various optical resonators and biosensing platforms. By precisely regulating the optical response of resonators, the application scenarios of optical sensing technology in biological detection have been greatly expanded. Among numerous technical routes of optical biosensing, resonant periodic nanostructures represented by gratings, metasurfaces, and photonic crystals occupy a dominant position due to their unique optical resonance response mechanisms. Such planar structures can form highly localized enhanced light fields through resonance effects, significantly strengthening the interaction between light and target biological substances, and thereby generating specific optical response signals that can be accurately captured. BICs hold substantial potential for enhancing sensing performance, attributed to their tunable high quality (Q)-factors and unique momentum-space polarization distributions.[27,28] However, their practical implementation is

AIP Publishing Applied Physics Reviews ACCEPTED MANUSCRIPT
This is the author's peer reviewed, accepted manuscript. However, the online version of record will be different from this version once it has been copyedited and typeset.
PLEASE CITE THIS ARTICLE AS DOI: 10.1063/5.0335616

hindered by significant bottlenecks: inherent structural defects in the fabrication process induce scattering losses, leading to a reduction in Q-factors. Traditional approaches such as increasing device size to suppress losses are constrained by nanomanufacturing precision and the physical limitations of mode volume. A recently proposed BIC merging strategy whereby multiple BICs are tuned to the same position in momentum space offers a novel approach to overcoming the Q factor limit. Nevertheless, current research primarily focuses on merging mechanisms based on intrinsic parameter variations of unit structures, relying on continuous structural parameter adjustments and faces challenges in efficiently integrating multiple BICs within a single model.[29-32] More importantly, the dynamic evolution of accidental BICs in experiments remains unclear, and their displacement characteristics induced by structural symmetry changes lack systematic characterization. Therefore, exploring more effective methods to enhance the Q factors of merged BICs and investigating the migration of accidental BICs are undoubtedly important directions worthy of further in-depth research.

In this work, we demonstrated that merging multiple accidental BICs with a SP-BIC at the Γ-point can further enhance the Q-factor at the Γ point, and the merged BICs exhibit robust tolerance to fabrication defects. Specifically, we designed an Al_2O_3 dielectric photonic crystal slab (PCS) supporting high-quality toroidal dipoles. Owing to the $C4_v$ symmetry of the PCS, a symmetry-protected BIC with a topological charge of +1 is observed at the Γ point, while additional accidental BICs are found at off-Γ points with wavevectors k_x and k_y. When the lattice period is varied, the SP-BIC remains fixed at the Γ point, whereas the accidental BICs at off-Γ points simultaneously move toward and merge at the Γ point. Further adjustment of the period causes the merged accidental BICs to separate along directions different from the merging path, posing challenges for achieving merged BICs through structural dimension optimization. To address this, we adjusted the symmetry of the PCS from $C4_v$ to $C6_v$. Merging multiple BICs with topological charges of ±1 results in a further 10^2-fold enhancement in the Q-factor, and the merged BICs remain in a stable merged state without separation upon structural variations, thereby improving optical response performance. Experimental results confirmed the merging process of the designed PCS, which is consistent with simulation outcomes, further validating our theoretical framework. This research fully demonstrates the enormous potential of merged BICs in optoelectronic devices and provides a new pathway for the development of high-performance optical response and high-precision detection technologies.

2. Design and Results

Figure 1 illustrates an efficient method for manipulating BICs. By tuning the unit cell period, the positions and evolution behaviors of BICs in momentum space can be precisely regulated. The symmetry arrangement of the PCS significantly influences the migration rules of BICs and the topological state evolution after their merging. This approach fully exploits the robustness and tunability of multiple BICs, which can notably enhance the overall efficiency and practicality of the optical response. We designed a dielectric Al_2O_3 circular pillar array with $C4_v$ symmetry on a near-air material substrate (ε_r=10). Its high dielectric constant enables the mode field to be localized within the pillars. Figure 2(a) presents the schematic diagram of the proposed structure in (upper panel), while the lower panel illustrates the structural parameters of the unit cell and the wave vector scanning region of the first Brillouin zone. The specific dimensions are: the period a = 4.43 mm, the circular pillar has a radius r = 1 mm, and the height h = 3 mm (The influence of the cylindrical dimensions on BICs is analyzed in Supporting Information 1).

AIP Publishing Applied Physics Reviews ACCEPTED MANUSCRIPT
This is the author's peer reviewed, accepted manuscript. However, the online version of record will be different from this version once it has been copyedited and typeset.
PLEASE CITE THIS ARTICLE AS DOI: 10.1063/5.0335616

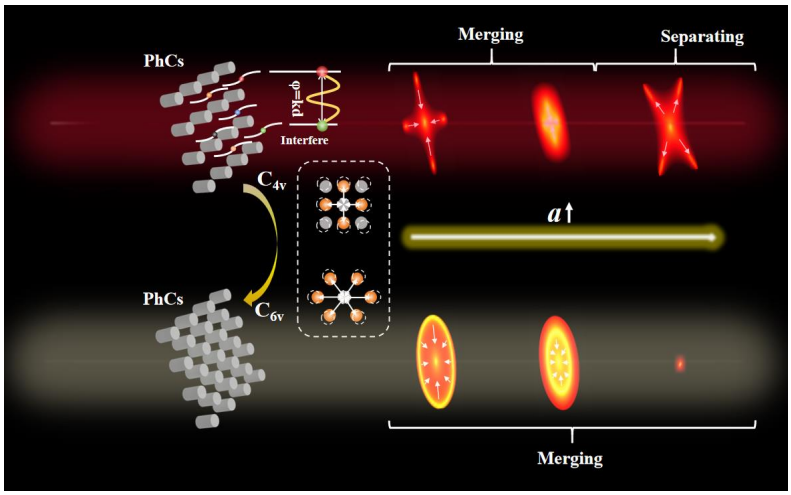


Figure 1. Schematic illustration of the BICs formation mechanism.

By calculating the effective refractive index $n_{eff}(\omega)$ beyond the long-wavelength limit,[33-34] we analyzed the equivalent wave velocity and dispersion characteristics of the mode (The calculation formula is provided in Supporting Information 2). It is confirmed that the symmetry-protected BIC arises from the complete closure of radiation channels due to symmetry incompatibility, and its effective refractive index exhibits flat dispersion at the Γ point, corresponding to an infinite quality factor. To investigate the mode distribution of BICs in C_{4v} symmetric PCS, we performed a systematic eigenmode analysis. For this structure, we calculated its band structure in the frequency range of 37-47 GHz by utilizing finite element analysis methods (COMSOL Multiphysics) and the results are presented in Fig. 2(b). Three distinct characteristic modes (Mode I, Mode II, and Mode III) can be clearly identified from the band structure. The positions marked by blue circles correspond to SP-BICs, which form at the Γ point. The physical essence of these BICs lies in the strict mismatch between mode symmetry and far-field radiation. Group theory analysis reveals that the irreducible representations of these modes do not overlap with those of far-field radiation, leading to complete suppression of radiation loss. In contrast, the positions marked by asterisks correspond to accidental BICs, which appear at off-Γ points. Accidental BICs originate from destructive interference between multiple resonant modes: when the radiation losses of multiple leaky modes satisfy specific coupling conditions, the total radiation loss can be canceled out, thereby forming bound states in the continuous spectrum. Displayed in the right-side insets are the visualized magnitude and vector profiles of the electric field (E) associated with the three modes at the $z = 0$ plane, with the border colors matching the respective band colors; notably, the electric field of Mode I exhibits localization behavior within the pillar structures, and its vector distribution exhibits a corresponding annular configuration. This finding demonstrates that within those multibound-state-assisted metasurfaces, the distributions of electric field are readily available to facilitate light-matter interaction—including optical trapping and biosensing implementations. Mode II presents the symmetric concentric circular distributions, and both the spatial extent and intensity of its electric field are significantly weaker than those of Mode I. In contrast, the electric

AIP Publishing Applied Physics Reviews ACCEPTED MANUSCRIPT
This is the author's peer reviewed, accepted manuscript. However, the online version of record will be different from this version once it has been copyedited and typeset.
PLEASE CITE THIS ARTICLE AS DOI: 10.1063/5.0335616

field of Mode III leaks outside the pillars, corresponding to a low-Q-factor mode in momentum space. The differences in electric field distributions intuitively reflect their symmetry and coupling characteristics in the band structure (Figures S2, Supporting Information 3). Further computations were carried out to derive the Q-factor distributions of the band structure for every mode along the high-symmetry paths, and these findings are depicted in Fig. 2(c). Mode I exhibits an infinitely large Q factor at the Γ point (SP-BIC), along with two additional Q factor peaks at off-Γ points (accidental BICs), indicating that this mode can support both types of BICs simultaneously. Mode II only has a SP-BIC. In contrast, the Q-factor of Mode III remains at a low level overall, behaving as an ordinary leaky mode with no significant BIC characteristics.

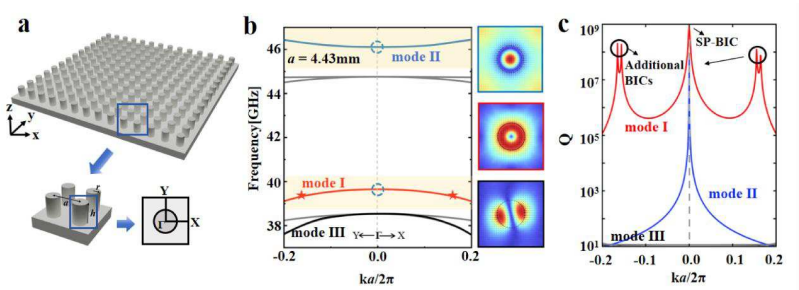


Figure 2. Eigenmode and BIC characteristics of the C4v-symmetric photonic crystal structure. (a) Schematic of the designed $C4_v$-symmetric photonic crystal structure. The structure consists of a periodic array of Al_2O_3 cylindrical pillars placed on a near-air dielectric substrate (ε_r = 10), with a lattice period of a = 4.43 mm, a pillar radius of r = 1 mm, and a height of h = 3 mm. The lower-left inset shows the local unit-cell structure and geometric parameters, while the lower-right inset illustrates the first Brillouin zone and the Y–Γ–X high-symmetry wave-vector scanning path. (b) Calculated band structure along the Y–Γ–X direction together with representative eigenmode electric-field distributions. The red, blue, and black bands correspond to Mode I, Mode II, and Mode III, respectively. The blue circles indicate SP-BICs at the Γ point, while the asterisks mark accidental BICs located away from the Γ point. The right-side insets show the corresponding electric-field distributions of the three modes in the z = 0 plane, with the border colors matching the respective band colors. (c) Q-factor curves of the three modes along the same high-symmetry path. Mode I supports one SP-BIC at the Γ point and two additional accidental BICs at off-Γ points; Mode II supports only one SP-BIC at the Γ point; Mode III exhibits an overall low Q factor and behaves as an ordinary leaky mode.

To elucidate the coupling mechanism between multiple accidental BICs and the SP-BIC located at the Γ point, we subsequently probed the evolutionary behaviors of Q factors and far-field radiation polarization profiles as a function of the lattice period a. The two-dimensional Q factor distribution maps corresponding to the band structures of Mode I and Mode II are displayed separately in Figs. 3(a) and 3(c). Specifically, Mode I features a single SP-BIC with a topological charge of +1 at the Γ point, along with four accidental BICs situated at off-Γ positions; by contrast, Mode II contains solely one SP-BIC at the momentum space center (i.e., the Γ point). As a is tuned from 4.43 mm to 4.81 mm, the four accidental BICs with a topological charge of -1 in Mode I shift gradually toward the Γ point, with their moving directions indicated by the white arrows in the figure, whereas the SP-BIC at the high-symmetry point in Mode II stays fixed and is unaffected by this period parameter. In a subsequent step, we uncovered the topological characteristics of BICs by computing the polarization distribution of far-field radiation. The

AIP Publishing Applied Physics Reviews ACCEPTED MANUSCRIPT
This is the author's peer reviewed, accepted manuscript. However, the online version of record will be different from this version once it has been copyedited and typeset.
PLEASE CITE THIS ARTICLE AS DOI: 10.1063/5.0335616

polarization vector of far-field radiation is defined as the projection of the Bloch wave function onto the planar basis vectors. Previous research has demonstrated that within the reciprocal space domain centered on BICs, the vector field assumes a vortex configuration, and

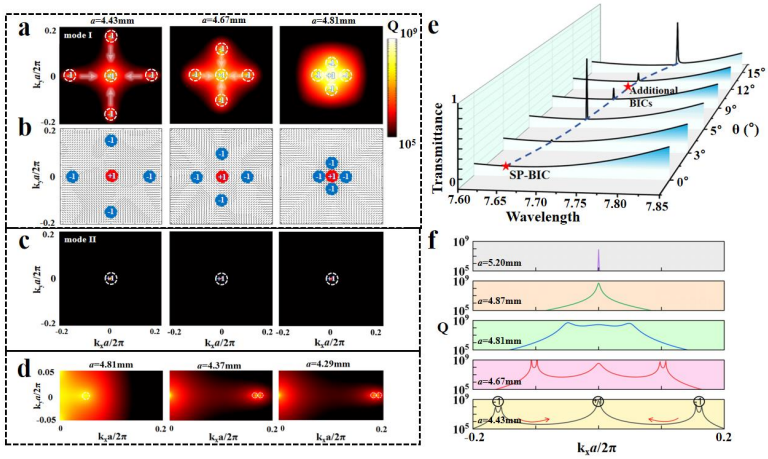


Figure 3. Merging of multiple accidental BICs with SP-BICs at the Γ point. Two-dimensional plots of the quality factor (Q-factor) as a function of lattice period a were calculated for the (a) Mode I and (c) Mode II bands. When period a is tuned from 4.43 mm to 4.81 mm, the BICs with ±1 topological charges in Mode I move toward the center, whereas the BIC at the high-symmetry point in Mode II remains unchanged. (b) Distribution of far-field polarization vectors around the BICs in the Mode I band. (d) During the merging process of Mode I, there are two accidental BICs at the off-Γ point, which will merge during their movement. (e) Schematic diagram of the transmittance of Mode I of the PCS with the increase of incident angle when a = 4.67 mm. The positions of BICs marked by asterisks in the figure are completely consistent with the characteristic positions of the Q-factor distribution. The dashed lines in the figure represent the offset trajectory of the resonant wavelength with the incident angle. (f) Variation of the Q factor along the $k_x a/(2\pi)$ direction as the lattice period a increases.

the topological charge q of the polarization vortex can be quantified by the number of phase rotation cycles over a closed loop. Leveraging the polarization distribution, we can directly visualize that all BIC points possess non-zero topological charges, as illustrated in Fig. 3(b); here, red and blue markers denote polarization singularities with topological charges of +1 and -1, respectively. For numerical calculation purposes, the topological charge can also be defined on the basis of the winding number of the polarization vector:

$$q = \frac{1}{2\pi}\oint_C dk \cdot \nabla_k \phi(k) \qquad (1)$$

where C is a counterclockwise closed loop surrounding the center of the topological vortex.[35] $\phi(k)=\arg[c_x(k)+ic_y(k)]$ is the polarization angle of the polarization vector at position k, $c_x(k)$ and $c_y(k)$ denote the electric field components along the x and y directions, respectively (Detailed calculations can be found in Supporting Information 4). As a increases, these singularities converge toward the Γ point, indicating a tendency for accidental BICs to merge with the SP-BIC. Figure 3(d) depicts the dynamic evolution of off-Γ BICs in Mode I as the a changes from 4.43 mm and 4.67 mm to 4.81 mm. When a = 4.43 mm, there are two separate accidental BICs, and the Q-

AIP Publishing Applied Physics Reviews ACCEPTED MANUSCRIPT
This is the author's peer reviewed, accepted manuscript. However, the online version of record will be different from this version once it has been copyedited and typeset.
PLEASE CITE THIS ARTICLE AS DOI: 10.1063/5.0335616

factor distribution shows two independent high-value regions. As a increases to 4.67 mm, the two BICs gradually approach each other, and the high-Q regions begin to overlap. When a = 4.81 mm, they are fully merged, forming an ultra-high Q peak concentrated near the Γ point. This process intuitively elucidates the merging mechanism of off- Γ BICs under lattice period modulation. We calculated transmission spectra of the metasurface at different incident angles when the a = 4.67 mm in Fig. 3(e). The blue dashed line shows the evolution of the q-BIC mode as a function of incident angle. Under normal incidence (θ = 0°), the ideal SP-BIC satisfies strict symmetry matching conditions, leading to complete suppression of radiative loss and full localization of energy within the metasurface. Accordingly, the transmission of the metasurface approaches 0. When the incident angle deviates from 0°, the in-plane symmetry of the metasurface is broken, and the ideal BIC transitions to a q-BIC, where radiative loss is gradually restored and transmission increases accordingly (e.g., at θ = 3°). The frequency of the q-BIC transmission peak undergoes a red shift with increasing incident angle, and the magnitude of the frequency shift becomes larger at higher angles (e.g., at θ = 5°). With a further increase in incident angle θ, the transmission decreases gradually, and the spectral linewidth of the resonance narrows (at θ = 9°). At an incident angle of θ = 9.3°, the transmission dip disappears entirely, indicating the formation of a true BIC mode (the red asterisk labeled "Additional BICs" corresponds to accidental BICs at off-Γ points). When θ continues to increase, the transmission dip reappears, marking the transition from a true BIC back to a q-BIC. Figure 3(e) reflects the continuous variation of transmission with wavelength and incident angle, while the transmission discontinuity at BIC positions confirms their angular selectivity. This result is fully consistent with the conclusions of the Q-factor distribution analysis discussed earlier. The Q-factor of the q-BIC mode at different incident angles can be obtained by

$$Q = \frac{\lambda_0}{\Delta\lambda}, \qquad (2)$$

where λ_0 denotes the resonant wavelength of the mode and $\Delta\lambda$ represents the full width at half maximum (FWHM) of the resonant mode.

The Q factor distributions of $C4_v$ structure are presented in the Γ-X direction as shown in Fig. 3(f). As the lattice period increases, the Q-factor peaks at off-Γ points gradually migrate toward the Γ point and converge into a single ultra-high Q factor peak at a = 4.81 mm. However, the Q factor at the high-symmetry point does not exhibit a significant increase compared with that before BIC merging; when the period further increases to 5.20 mm, the Q factor at this high-symmetry point even decreases. To explain this special phenomenon, we calculated the two-dimensional Q-factor distribution maps and far-field polarization vector distributions of Mode I at lattice constant a = 4.87 mm, 4.91 mm, and 5.20 mm, as shown in Figs. 4(a) and 4(b). When a exceeds the merging point, the accidental BICs previously merged at the Γ point migrate diagonally, as shown by the white arrows in the figure, while retaining their original topological charges (±1). At a = 4.87 mm, multiple accidental BICs gather around the SP-BIC at the Γ point, with polarization singularities (marked as -1) densely distributed in the central region. As a increases to 4.91 mm, these accidental BICs continue to separate and move along the diagonal direction. At a = 5.20 mm, the accidental BICs have completely separated from the Γ point, forming symmetrically distributed polarization singularities at off-Γ positions, while the SP-BIC remains at the center with a +1 topological charge. This phenomenon indicates that lattice period engineering allows for both merging and separation of BICs. Notably, the transition from BIC coalescence to separation

AIP Publishing Applied Physics Reviews ACCEPTED MANUSCRIPT
This is the author's peer reviewed, accepted manuscript. However, the online version of record will be different from this version once it has been copyedited and typeset.
PLEASE CITE THIS ARTICLE AS DOI: 10.1063/5.0335616

is abrupt, making it challenging to pinpoint the exact parameter values at which multiple BICs fully merge. Figure 4(c) presents the two-dimensional transmission spectrum as a function of wavelength λ and incident angle θ when a = 5.20 mm. Only the transmission dip at θ = 0° corresponds to the SP-BIC at the Γ point, exhibiting a complete transmission suppression effect. This characteristic further verifies that there is a significant difference between the separation path of accidental BICs and SP-BICs and their merging path. In addition, the height and radius of the cylinder can also provide new degrees of freedom for BIC manipulation (Figs. S3 and S4, Supporting Information 5).

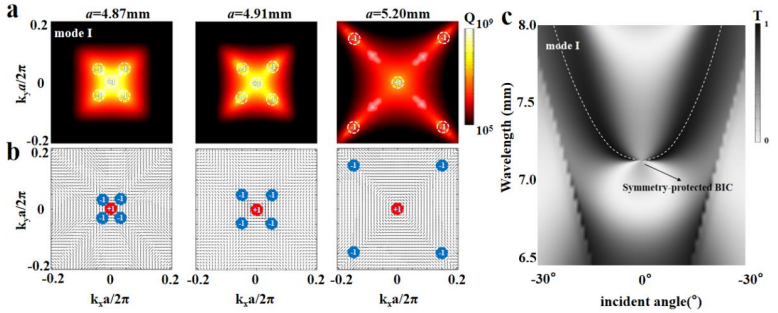


Figure 4. Separation of multiple accidental BICs from SP-BICs. (a) When the lattice period continues to increase, the accidental BICs that have merged to the Γ point move diagonally while carrying their original topological charges. (b) Corresponding far-field polarization vector distributions, showing the positional evolution of the accidental BICs, while the SP-BIC remains at the Γ point. (c) Two-dimensional transmission spectrum was calculated when a = 5.20 mm.

To observe the displacement of BICs in momentum space, the symmetric metasurface structure with a 14×14 array scale was fabricated in this study. Figure 5(a) shows the photograph of the dielectric Al_2O_3 cylinders used in the experiment, whose unit structures are periodically and orderly arranged (Fig. S5 in the Supporting Information 6). Figure 5(b) presents the schematic diagram of the experimental sample, which integrates core components including detection holes, wave-absorbing materials, and an air substrate. This configuration can minimize background signal interference and ensure the accuracy of characterization data. In the experiment, we first obtained the near-field amplitude and phase distributions of the finite photonic-crystal slab in real space (x, y), and mapped them to the in-plane momentum space (k_x, k_y) via a two-dimensional Fourier transform.

$$F(\mathrm{k}_u,\mathrm{k}_v)=\sum_{m=0}^{M-1}\sum_{n-0}^{N-1} f(\mathrm{x}_m,\mathrm{y}_n)\mathrm{e}^{-i2\pi\left(\frac{k_u m}{M}+\frac{k_v n}{N}\right)}, \quad (3)$$

where $f(x_m, y_n)$ denotes the two-dimensional discrete signal in the spatial domain. Furthermore, the resonant wavelength λ_0 and full-width at half-maximum $\Delta\lambda$ at each momentum point were further extracted, and the corresponding Q-factors were calculated according to $Q = \lambda_0 / \Delta\lambda$ to obtain the final result (λ_0 = 7.56 mm). Figure 5(c) displays the simulated (upper row) and experimental (lower row) Q-factor distribution maps at lattice constants a = 4.43 mm, 4.67 mm, and 4.87 mm, clearly revealing that the Q-factor distributions are in good agreement with the simulation results, as a increases, the Q-factor maps of both exhibit consistent evolution trends in the migration and

AIP Publishing Applied Physics Reviews ACCEPTED MANUSCRIPT
This is the author's peer reviewed, accepted manuscript. However, the online version of record will be different from this version once it has been copyedited and typeset.
PLEASE CITE THIS ARTICLE AS DOI: 10.1063/5.0335616

merging processes of BIC modes, with their Q-factor peaks reaching 1.1×10^4 at 39 GHz. Notably, the scale of the metasurface array is one of the key factors affecting the experimental measurement results, and we performed simulation calculations on crystal plates with array scales of 9×9, 14×14 and 20×20. Limited by the preparation conditions, the Q factor of the 14×14-array PCS prepared in the experiment deviates from the simulated value by up to two orders of magnitude. In addition, the depth at which the probe is inserted into the detection hole and the placement angle of the excitation source relative to the PCS can jointly induce a reduction in the Q factor. The aforementioned factors together constitute the core reasons for the deviation between the experimental data and the simulation results(Fig. S6 in the Supporting Information 7).

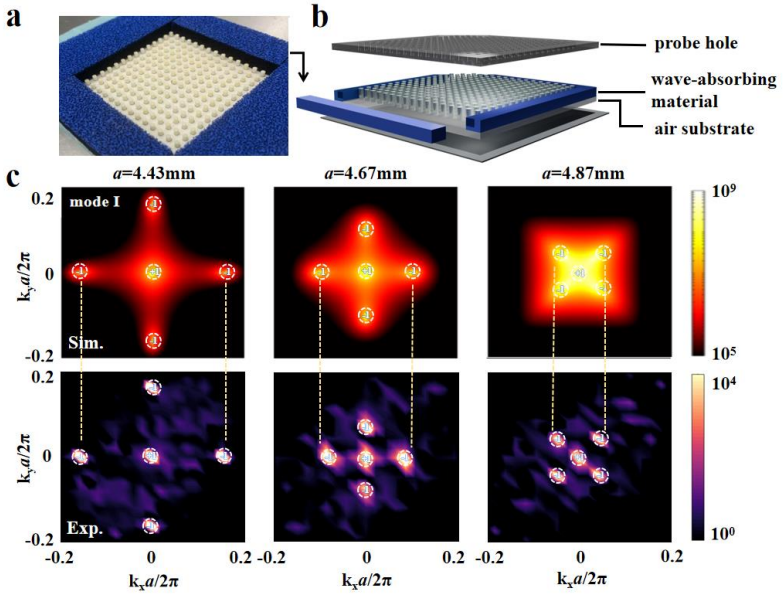


Figure 5. Experimental observation of BIC displacement. (a) Photograph of the experimentally fabricated metasurface sample, showing the appearance of an Al_2O_3-based photonic crystal with a periodically arranged structure; Panel (b) is a schematic diagram of its structure, clearly showing components such as the probe hole, wave absorbing material, and air substrate. Panels (c) respectively show the Q-factor distributions obtained from experiments and simulations under different lattice constants (a = 4.43 mm, a = 4.67 mm, a = 4.87 mm). It can be found that the experimental results are basically consistent with the simulation results.

To precisely achieve the merging of multiple BICs, we arranged the Al_2O_3 cylinder with identical parameters into the $C6_v$ symmetric array in Fig. 6(a). We calculated the band structure at a lattice constant of a = 3.48 mm, and the results are presented in Fig. 6(b). Two distinct characteristic modes (Mode I and Mode II) were identified from the band diagram. The position marked by the blue circle corresponds to the SP-BIC formed. This BIC shares the same fundamental physical origin as that in the $C4_v$ structure, both arising from a strict mismatch between mode symmetry and far-field radiation. However, the $C6_v$-structure possesses a higher symmetry, which imposes more stringent matching criteria on its irreducible representations, thereby enhancing the stability of the radiation suppression effect of the SP-BIC. The positions

AIP Publishing Applied Physics Reviews ACCEPTED MANUSCRIPT
This is the author's peer reviewed, accepted manuscript. However, the online version of record will be different from this version once it has been copyedited and typeset.
PLEASE CITE THIS ARTICLE AS DOI: 10.1063/5.0335616

marked by asterisks denote accidental BICs. Notably, governed by the hexagonal lattice symmetry, accidental BICs in the six-fold rotationally symmetric structure exhibit a six-fold symmetric distribution, in contrast to the four-fold symmetric distribution observed in the $C4_v$-structure. The insets of Fig. 6(b) illustrate the electric field distributions and vector field profiles of the two modes in the $z = 0$ plane. Specifically, the electric field energy of Mode I is efficiently confined within the unit structure, with its vector distribution exhibiting an annular configuration. In contrast, the electric field of Mode II escapes from the unit structure, and this distribution characteristic is similar to that of Mode III in the $C4_v$-structure. Figure 6(c) depicts the Q-factor distributions of the two modes. Mode I comprises one SP-BIC and two accidental BICs, following a distribution consistent with that of Mode I in the $C4_v$-structure. In contrast, Mode II is categorized as a low-Q leaky mode and does not exhibit obvious BIC characteristics.

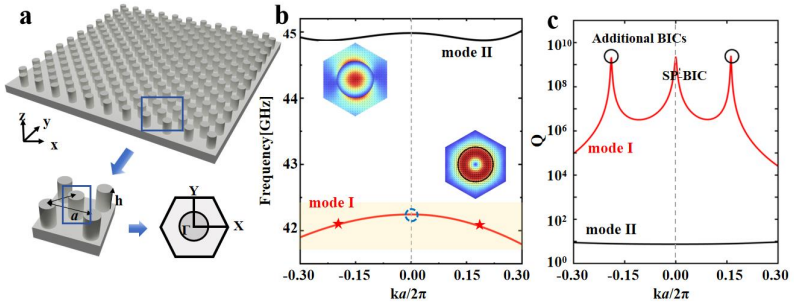


Figure 6. Eigenmode analysis of the $C6_v$ structure. (a) Schematic diagram of the designed $C6_v$-structured PCS. On the left side of the lower figure is a schematic of 5 intercepted unit cells. Except for the lattice period a, the structural parameters of this structure are the same as those of the $C4_v$ structure. On the right side is a schematic of the first Brillouin zone.(b) In the frequency range from 41 GHz to 45.5 GHz, when the lattice constant a is 3.48 mm, the band structure of the Al_2O_3 resonant cavity in the hexagonal lattice along the Y-Γ-X direction is simulated and calculated. The positions of the asterisks correspond to the two accidental BICs, and the blue circles mark the positions of the SP-BICs. The inset shows the electric field distributions of the two modes on the $z = 0$ plane.(c) The Q-factor distributions of the band structures of these two modes along the high-symmetry line with respect to $ka/2\pi$ are simulated. The results reveal that Mode I has one SP-BIC at the high-symmetry point and two accidental BICs at off-Γ points. Mode II is a low-Q leaky mode.

The SP-BIC and accidental BICs in Mode I carry topological charges of +1 and ±1, so we aimed to achieve the merging of multiple BICs of Mode I. While the SP-BIC is anchored at the Γ point, the accidental BICs allow position adjustment via structural parameter tuning. As shown in Fig. 7(a), with $r = 1$ mm and $h = 3$ mm fixed, increasing a from 3.48 mm to 3.81 mm can drive the accidental BICs chain to approach and merge with the SP-BIC. At this point, the topological charges of opposite signs annihilate, and only the merged BICs with a topological charge of +1 remain at the Γ point. This phenomenon demonstrates that the accidental BICs have been fully integrated into the SP-BIC, with the Q factor reaching up to 4.169×10^{10}. Upon increasing the period to $a = 5.21$ mm (as shown in the right panel of Fig. 7a), the merged BICs remain in a stable merged configuration. In addition to the lattice period, adjusting the structural height h can also regulate the positions of BICs of Mode I when the lattice period a is fixed at 3.48 mm. When h decreases from 3.00 mm to 2.89 mm, the high-Q regions corresponding to BICs gradually contract

AIP Publishing Applied Physics Reviews ACCEPTED MANUSCRIPT
This is the author's peer reviewed, accepted manuscript. However, the online version of record will be different from this version once it has been copyedited and typeset.
PLEASE CITE THIS ARTICLE AS DOI: 10.1063/5.0335616

toward the Γ point (Fig. 7(b)), which directly reflects the regulatory effect of structural height on the BIC localization characteristics and Q factor enhancement effect. Figure 7(c) compares the simulated (upper panel) and experimental (lower panel) Q-factor distributions under the conditions of a = 5.21 mm and h = 3.00 mm. Both the experimental and simulated results show a significant high-Q region at the Γ point with high consistency, which verifies the reliability of the structural design scheme and characterization methods in this study. The peak Q-factor measured experimentally reaches 2.67×10^4 at 38.1 GHz. It should be noted that the maximum emission frequency of the excitation source in this study is 40 GHz. Therefore, the structural period was adjusted to a = 5.21 mm to reduce the resonant frequency to 38.1 GHz. The corresponding calculated Q factor reaches 6.25×10^9. In accordance with theoretical predictions, the experimentally measured Q-factor can reach 10^5 when the structural period is set to a = 3.81 mm. Figure 7(d) shows the variation curves of the Q factor along the $k_xa/(2\pi)$ direction for different a. As a increases, both peaks of Q factor migrate toward the center and this migration is fully consistent with the BIC merging behavior observed in Fig. 7(a), further confirming the evolution law of BICs under period regulation.

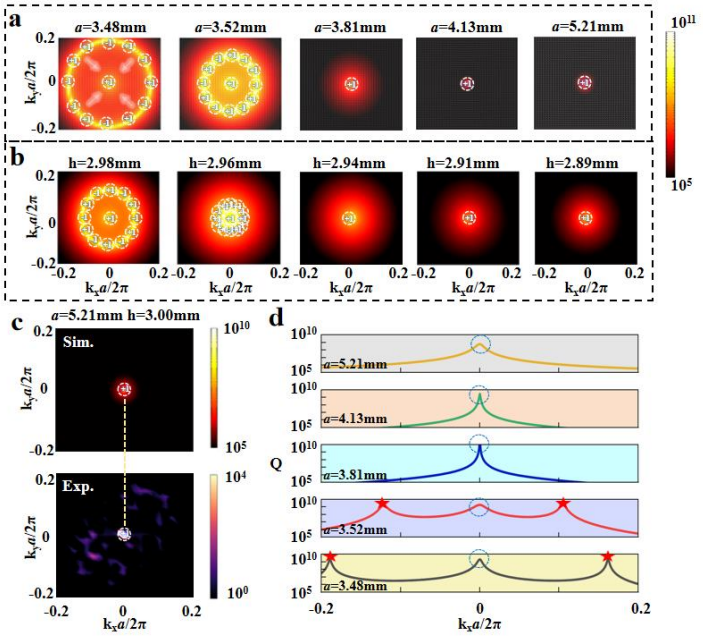


Figure 7. Tuning of BICs via lattice period a and height h. (a) Two-dimensional Q-factor maps of Mode I under different a (with fixed height h = 3.00 mm). (b) Two-dimensional Q-factor maps of Mode I under different heights h (with fixed a = 3.48 mm). (c) Comparison of experimental and simulated Q-factor distributions for a = 5.21 mm and h = 3.00 mm. (d) Variation of Q-factor along $k_xa/(2\pi)$ for different lattice periods a.

We further quantified and contrasted the Q-factor evolution of the $C4_v$ (red curve) and $C6_v$ (blue curve) structures in Fig. 8(a) to clearly compare the influence of different symmetric structures on the magnitude of the Q factor. The results show that the Q factor of the $C6_v$ structure

AIP Publishing Applied Physics Reviews ACCEPTED MANUSCRIPT
This is the author's peer reviewed, accepted manuscript. However, the online version of record will be different from this version once it has been copyedited and typeset.
PLEASE CITE THIS ARTICLE AS DOI: 10.1063/5.0335616

can be significantly enhanced to 10^{10}, while the Q factor of the $C4_v$ structure remains consistently at 10^8. Such a discrepancy in Q factor can be explained by the coupled-mode theory (CMT). Based on the CMT, off-Γ BICs originate from the coupling of all waves in all channels (including in-plane closed channels and out-of-plane radiation channels), and all waves coupled into the open channels undergo destructive interference.[36-37] The CMT equation can be expressed as:

$$\frac{dA}{dt} = i\omega_0 A + i\sum_i \kappa_j A_j - (\frac{\omega_0}{2Q} + \frac{\omega_0}{2Q_n})A \quad (4)$$

where A is the amplitude of the dark mode, A_j is the amplitude of the j-th radiative bright mode, Q is the radiative quality factor caused by leakage into free space, and Q_n is the normalized non-radiative quality factor which is related to material absorption and scattering, and not directly affected by symmetry.[38] From the perspective of CMT, the Q factor of BIC is directly determined by the radiation loss γ_{rad}, and the quantitative relationship between them is $Q = \omega_0/(2\gamma_{rad})$, where ω_0 is the eigenfrequency of BIC. The magnitude of the radiation loss γ_{rad} depends on the superposition of the coupling coefficients between the dark mode and all radiative bright modes. In the equation, κ_j is the coupling coefficient between the dark mode and the j-th radiative mode, and its value is determined by the symmetry matching degree between the dark mode and the radiative mode. If the structural symmetry results in symmetry incompatibility between the two modes, $\kappa_j = 0$. Conversely, the higher the degree of symmetry matching, the larger the value of κ_j. Ultimately, the radiation loss can be simplified to, $\gamma_{rad} = \sum_j|\kappa_j|^2$ the sum of the squares of the coupling coefficients directly determines the intensity of radiation loss, that is, $Q = \omega_0/(2\sum_j|\kappa_j|^2)$.

Based on the above CMT of the SP-BICs, the total radiation loss can be reduced and the Q factor of the mode can be enhanced by increasing the constraint dimension of radiation channels and reducing the number of κ_j that meet the symmetry matching requirement. Figure 8(b) shows that the designed $C4_v$ metasurface can constrain radiation channels in 4 directions. The coupling inhibition of its BIC mode depends on a single symmetric superposition condition such as rotational symmetry and inversion symmetry, and only part of the radiation channels can be blocked from coupling. The number of κ_j satisfying symmetry matching is relatively large, which causes some κ_j to change from 0 to non-zero, making it difficult to further reduce the total radiation loss γ_{rad}. Therefore, the Q factor of $C4_v$ obtained by simulation is limited to the order of 10^8. Affected by the perturbations of the structure and the excitation source in experiments, the actual Q factor is at the order of 10^4, and the Q factor will decrease significantly when the degree of symmetry breaking (incident angle) increases. In contrast, the $C6_v$ metasurface possesses a higher order of symmetry and can constrain radiation channels in 6 directions as shown in Fig. 8(b). Moreover, its BIC mode is protected by multiple simultaneous symmetry conditions (e.g., rotation, inversion, and mirror symmetry). A coupling coefficient κ_j becomes non-zero only when all these symmetries are broken concurrently. This multi-dimensional constraint greatly reduces the number of κ_j satisfying symmetry matching, so that the total radiation loss γ_{rad} can be reduced to below 10^{-10} rad/s, and the theoretical upper limit of the corresponding Q factor can reach the order of 10^{10}-10^{11}. Furthermore, the high symmetry of the $C6_v$ photonic crystal enables the structure to maintain most $\kappa_j = 0$ even under slight perturbations, such as lattice scaling or hole position deviation, resulting in a slow decay of the Q factor. This unique property ensures that the merged BICs remain invariant with respect to the lattice period a.

AIP Publishing
Applied Physics Reviews ACCEPTED MANUSCRIPT
This is the author's peer reviewed, accepted manuscript. However, the online version of record will be different from this version once it has been copyedited and typeset.
PLEASE CITE THIS ARTICLE AS DOI: 10.1063/5.0335616

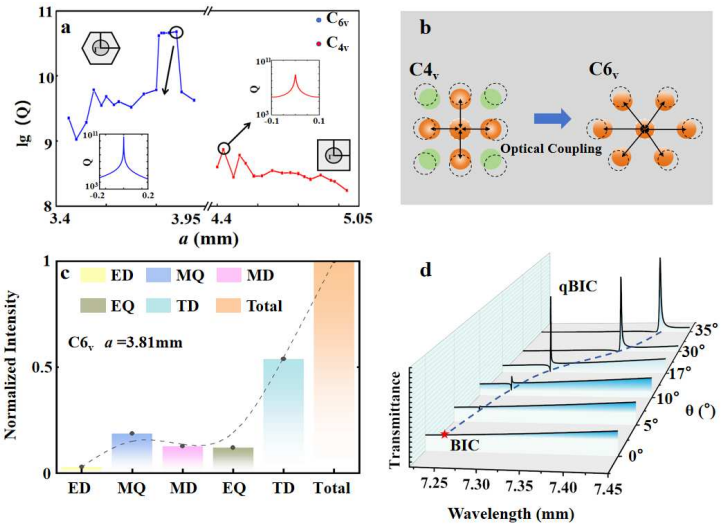


Figure 8. Comparison of the effects of different symmetric structures on quality factors. (a) Schematic diagram of coupling between $C4_v$ and $C6_v$ symmetric structures. (b) Comparison of Q-factors between the $C4_v$ and $C6_v$ structures. The blue line represents the $C6_v$ structure and the red line represents the $C4_v$ structure. (c) Multipole decomposition analysis reveals that the selected bands are predominantly influenced by a toroidal dipole mode. The abbreviations ED, MD, TD, EQ and MQ denote electric dipole, magnetic dipole, toroidal dipole, electric quadrupole, and magnetic quadrupole, respectively. (d) Transmittance of PCS as the incident angle increases when a = 3.81 mm. The positions of BICs are marked with asterisks in the figure, and the dashed lines represent the offset trajectory of the resonant wavelength with the incident angle.

Through the multipole decomposition analysis in Fig. 8(c), it can be confirmed that corresponding to the toroidal distribution of the electric field, the electromagnetic response of the target band is dominated by the toroidal dipole (TD) mode, while the contributions of other multipoles such as the electric dipole (ED) and magnetic dipole (MD) are relatively weak (the calculation of multipole decomposition is shown in the Supporting Information 8). Figure 8(d) illustrates the transmittance characteristics of the PCS as a function of the incident angle (with a=3.81 mm). Asterisks mark the positions of BICs, and the dashed lines represent the shift trajectory of the resonant wavelength with the incident angle. As the incident angle increases, the resonant peak undergoes a redshift but still maintains a distinct response, which reflects the angular robustness of the merged BICs. Herein, we analyzed its sensing performance to conduct an in-depth analysis of the optical response characteristics of the $C6_v$-symmetric dielectric metasurface, with the relevant results presented in Figure 9. By modulating the background refractive index, we simulated the influence of different environments on the qBIC resonance characteristics, with the results presented in Fig. 9(a). The baseline background was set as air (n_B = 1). Regarding the selection of the incident angle, although a smaller incident angle θ leads to a higher Q factor and a narrower resonance linewidth, the signal amplitude of the resonance peak decreases synchronously. When $\theta = 0°$, the resonance peak even disappears completely (Fig. 8(d)),

AIP Publishing Applied Physics Reviews ACCEPTED MANUSCRIPT
This is the author's peer reviewed, accepted manuscript. However, the online version of record will be different from this version once it has been copyedited and typeset.
PLEASE CITE THIS ARTICLE AS DOI: 10.1063/5.0335616

which is unfavorable for practical detection. For this reason, we selected an incident angle of θ = 17°. The schematic diagram of the designed sensor is shown in the inset of Figure 9(b). Impurity units and Al_2O_3 functional structures are distributed in the detection environment. As the background refractive index increases, the transmission peak in the transmission spectrum exhibits a significant redshift, as shown in Fig. 9(a). This is because an increase in the background refractive index elevates the overall effective refractive index of the metasurface structural units. To further investigate the sensor performance, we analyzed the variation of the resonance peak frequency (ω_{dip}) and the full width at half maximum (FWHM) of the transmission spectrum with respect to n_B. The results are displayed in Fig. 9(b). Both ω_{dip} and FWHM show a linear dependence on n_B. This linear dependence can be utilized to achieve sensing detection of the refractive index of biological components. Sensitivity S is a core metric for evaluating the performance of refractive index sensors, which is defined as $S = \Delta\lambda/\Delta n_B$ (where $\Delta\lambda$ is the shift of the resonant wavelength, Δn_B is the variation of the background refractive index, with the unit of μm/RIU). Figure 9(c) presents the variation trend of the sensitivity. Combined with the fitting curve, it can be concluded that within the tested refractive index range, the sensitivity maintains a stable variation trend with n_B, which provides a reliable performance basis for the application of this sensor in scenarios with different refractive indices.

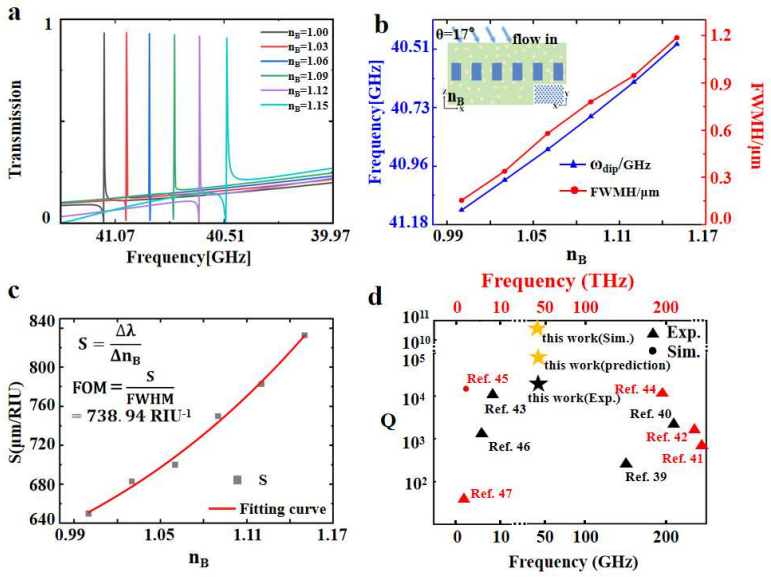


Figure 9. Sensing performance analysis. (a) Transmission spectra under different background refractive indices. The schematic diagram of the designed sensor is shown in the inset of panel (b). (b) Resonant frequency and FWHM with background refractive index. (c) Calculation and linear fitting of sensitivity S as a function of background refractive index. (d) Comparison of operating wavebands and Q factors of different metasurfaces.

A comparison of the Q-factors between the metasurface structure proposed in this paper and those reported in existing literature is presented in Fig. 9(d).[39-47] Here, the red literature labels correspond to the terahertz band on the upper horizontal axis of the figure, while the black

AIP Publishing Applied Physics Reviews ACCEPTED MANUSCRIPT
This is the author's peer reviewed, accepted manuscript. However, the online version of record will be different from this version once it has been copyedited and typeset.
PLEASE CITE THIS ARTICLE AS DOI: 10.1063/5.0335616

literature labels correspond to the gigahertz band on the lower horizontal axis. It can be clearly seen from the figure that both the simulation (yellow pentagram) and experimental (black pentagram) data show that the Q factor of the structure designed in this paper is higher than that of structures reported in other literature in the corresponding bands, demonstrating a prominent performance advantage. Meanwhile, as an optical platform in free space, this metasurface provides greater convenience for the regulation of optical responses.

3. Conclusions

We conducted a systematic investigation of the merging mechanism, regulation strategy, and sensing application potential of BICs. A $C4_v$-symmetric Al_2O_3-based PCS structure was designed and fabricated. Eigenmode analysis and finite-element simulations clarified the distribution of three characteristic modes. These analyses confirmed an SP-BIC with a topological charge of +1 at the Γ point and accidental BICs at off-Γ points originating from destructive interference between multiple resonant modes. The radiation loss characteristics of different modes were revealed through electric field distribution and Q-factor analysis. It was found that increasing the period can drive off-Γ accidental BICs to migrate toward the Γ point and merge with the SP-BIC, forming an ultra-high Q-factor peak. However, further increasing the period causes the merged BICs to separate along the diagonal direction, and the separation path is significantly different from the trajectories. To stabilize the merged state, an optimization scheme of adjusting the structural symmetry from $C4_v$ to $C6_v$ was proposed. Utilizing the stronger light field confinement capability and mode interference suppression effect of six-fold symmetry, stable merging of accidental BICs and SP-BIC was achieved. Following topological-charge annihilation, a net charge of +1 remains, accompanied by a significant enhancement in the Q factor (up to 10^{10}). Meanwhile, it was confirmed that the structural height can also regulate the localization characteristics and Q-factor enhancement effect of BICs. In addition, experimental verification was carried out by fabricating an Al_2O_3-based metasurface sample with a 14×14 array scale. The measured Q-factor distribution is in good agreement with the simulation results, verifying the reliability of the theoretical framework. To match the excitation source frequency, the lattice period was tuned, thereby adapting the resonance to experimental conditions. This further confirmed the robustness of the merged BICs to period variations. This study clarifies the regulation mechanism of structural parameters and symmetry on the merging-separation evolution of BICs. The proposed stable BIC merging strategy effectively breaks through the bottlenecks of limited Q-factor and sensitivity to fabrication defects in traditional BIC applications, and provides a new idea and experimental basis for the development of high-performance photonic sensing, high-precision detection and other technologies.

Supporting Information

The theoretical derivations and detailed experimental measurement protocols adopted in this work are comprehensively elaborated in the Supporting Information, with specific contents organized as follows: (1) Mechanistic investigation into the hybridization of BIC modes controlled and tuned by elliptical cylinder dielectric structures; (2) In-depth theoretical analysis and quantitative calculation of the effective refractive index for the symmetric dielectric metasurface structures employed in this study; (3) Electric and magnetic field mode distributions and vector characteristics of the designed $C4_v$ and $C6_v$ symmetric structures at multiple representative cross-sections; (4) Systematic numerical derivation and topological characterization of the far-field

AIP Publishing Applied Physics Reviews ACCEPTED MANUSCRIPT
This is the author's peer reviewed, accepted manuscript. However, the online version of record will be different from this version once it has been copyedited and typeset.
PLEASE CITE THIS ARTICLE AS DOI: 10.1063/5.0335616

polarization states and polarization vortex distributions around BIC points; (5) Parametric regulation mechanism and quantitative analysis of the optical quality (Q) factor with respect to the radius and height of the dielectric cylindrical elements; (6) Complete and detailed procedures for the experimental setup construction, sample preparation, microfabrication, and structural characterization; (7) Comparative analysis and error discussion between the experimentally measured results and numerically simulated theoretical values; (8) Theoretical analysis of multilevel decomposition; (9) Supplementary figures (Fig.S1–S6) that provide intuitive visualization, data support, and supplementary verification for the above theoretical analysis, numerical simulations, and experimental measurements.

Acknowledgments

This work is supported by the National Key Research and Development Program of China (2024YFE107800); Basic Research Program of Jiangsu (BK20231493); National Natural Science Foundation of China (12574477).

AIP Publishing Applied Physics Reviews ACCEPTED MANUSCRIPT
This is the author's peer reviewed, accepted manuscript. However, the online version of record will be different from this version once it has been copyedited and typeset.
PLEASE CITE THIS ARTICLE AS DOI: 10.1063/5.0335616

Reference

1. Y. Plotnik, O. Peleg, F. Dreisow, M. Heinrich, S. Nolte, A. Szameit, and M. Segev, "Experimental observation of optical bound states in the continuum," Phys. Rev. Lett. **107**, 183901 (2011).
2. D. C. Marinica, A. G. Borisov, and S. V. Shabanov, "Bound states in the continuum in photonics," Phys. Rev. Lett. **100**, 183902 (2008).
3. S. Longhi and G. D. Valle, "Floquet bound states in the continuum," Sci. Rep. **3**, 2219 (2013).
4. J. Zhang, D. Braak, and M. Kollar, "Bound states in the continuum realized in the one-dimensional two-particle Hubbard model with an impurity," Phys. Rev. Lett. **109**, 116405 (2012).
5. J. Li, J. Li, C. Zheng, Z. Yue, D. Yang, S. Wang, M. Li, Y. Zhang, and J. Yao, "Spectral amplitude modulation and dynamic near-field displaying of all-silicon terahertz metasurfaces supporting bound states in the continuum," Appl. Phys. Lett. **119**, 241105 (2021).
6. P. P. Vabishchevich, S. Liu, M. B. Sinclair, G. A. Keeler, G. M. Peake, and I. Brener, "Enhanced second-harmonic generation using broken symmetry III–V semiconductor Fano metasurfaces," ACS Photonics **5**, 1685-1690 (2018).
7. N. Muhammad, Y. Chen, C. Qiu, G. Wang, "Optical bound states in continuum in MoS2-based metasurface for directional light emission," Nano Lett. **21**, 967-972 (2021).
8. X. Zhao, C. Chen, K. Kaj, L. Hammock, Y. Huang, R. D. Averitt, X. Zhang, "Terahertz investigation of bound states in the continuum of metallic metasurfaces," Optica **7**, 1548-1554 (2020).
9. R. Liu and C. Zhou, "Second harmonic generation in an anisotropic lithium niobate metasurface governed by quasi-BICs," Opt. Lett. **48**, 6565-6568 (2023).
10. H. Duan, H. He, Y. Yi, L. Wang, Y. Zhang, S. You, Y. Wang, C. Gao, J. Huang, and C. Zhou, "Efficient second-harmonic generation in a lithium niobate metasurface governed by high-Q magnetic toroidal dipole resonances," Opt. Lett. **49**, 5539-5542 (2024).
11. S. You, H. He, Y. Zhang, H. Duan, L. Wang, Y. Wang, S. Luo, and C. Zhou, "Resonance wavelength stabilization of quasi-bound states in the continuum constructed by symmetry breaking and area compensation," Nano Lett. **24**, 15300-15307 (2024).
12. C. W. Hsu, B. Zhen, A. D. Stone, J. D. Joannopoulos, and M. Soljačić, "Bound states in the continuum," Nat. Rev. Mater. **1**, 16048 (2016).
13. V. R. Tuz, V. V. Khardikov, A. S. Kupriianov, K. L. Domina, S. Xu, H. Wang, and H.-B. Sun, "High-quality trapped modes in all-dielectric metamaterials," Opt. Express **26**, 2905-2916 (2018).
14. V. A. Fedotov, M. Rose, S. L. Prosvirnin, N. Papasimakis, and N. I. Zheludev, "Sharp trapped-mode resonances in planar metamaterials with a broken structural symmetry," Phys. Rev. Lett. **99**, 147401 (2007).
15. J. Tian, Q. Li, P. A. Belov, R. K. Sinha, and W. Qian, "High-Q all-dielectric metasurface: Super and suppressed optical absorption," ACS Photonics **7**, 1436-1443 (2020).
16. A. S. Kupriianov, Y. Xu, A. Sayanskiy, V. Dmitriev, Y. S. Kivshar, and V. R. Tuz, "Metasurface engineering through bound states in the continuum," Phys. Rev. Appl. **12**, 014024 (2019).

AIP Publishing Applied Physics Reviews ACCEPTED MANUSCRIPT
This is the author's peer reviewed, accepted manuscript. However, the online version of record will be different from this version once it has been copyedited and typeset.
PLEASE CITE THIS ARTICLE AS DOI: 10.1063/5.0335616

17. D. R. Abujetas, Á. Barreda, F. Moreno, A. Litman, J.-M. Geffrin, and J. A. Sánchez-Gil, "High-Q transparency band in all-dielectric metasurfaces induced by a quasi bound state in the continuum," Laser & Photonics Rev. **15**, 2000263 (2021).
18. S. Murai, D. R. Abujetas, G. W. Castellanos, J. A. Sánchez-Gil, F. Zhang, and J. G. Rivas, "Bound states in the continuum in the visible emerging from out-of-plane magnetic dipoles," ACS Photonics **7**, 2204-2210 (2020).
19. S. Xiao, T. Liu, X. Wang, X. Liu, and C. Zhou, "Tailoring the absorption bandwidth of graphene at critical coupling," Phys. Rev. B **102**, 085410 (2020).
20. N. J. J. van Hoof, D. R. Abujetas, S. E. T. ter Huurne, F. Verdelli, G. C. A. Timmermans, J. A. Sánchez-Gil, and J. Gómez Rivas, "Unveiling the symmetry protection of bound states in the continuum with terahertz near-field imaging," ACS Photonics **8**, 3010-3016 (2021).
21. J. Guo, R. Jin, Z. Fu, Y. Zhang, F. Yu, J. Chen, X. Wang, L. Huang, C. Zhou, X. Chen, W. Lu, and G. Li, "Topologically engineered high-Q quasi-BIC metasurfaces for enhanced near-infrared emission in PbS quantum dots," Nano Lett. **25**, 2357–2365 (2025).
22. Y. Li, Y. Sun, W. Zhu, Z. Guo, J. Jiang, T. Kariyado, H. Chen, and X. Hu, "Topological LC-circuits based on microstrips and observation of electromagnetic modes with orbital angular momentum," Nat. Commun. **9**, 4598 (2018).
23. S. Hu, Z. Guo, W. Liu, S. Chen, and H. Chen, "Hyperbolic metamaterial empowered controllable photonic Weyl nodal line semimetals," Nat. Commun. **15**, 2773 (2024).
24. H. Sun, W. Wu, Z. D. Hu, W. Yu, J. Wu, and J. Wang, Y. Yang, M. Li, and S. Khakhomov, "High-capacity corner state encoding and dual-plane switching encryption based on topological photonic crystals," Laser & Photonics Rev. **19**, e01103 (2025).
25. J. Zhang, Y. Ruan, Z. D. Hu, J. Wu, and J. Wang, "An enhanced high Q-factor resonance of quasi-bound states in the continuum with all-dielectric metasurface based on multilayer film structures," IEEE Sensors J. **23**, 2070-2075 (2023).
26. L. Yang, J. Wang, L. Z. Yang, Z.-D. Hu, X. Wu, and G. Zheng, "Characteristics of multiple Fano resonances in waveguide-coupled surface plasmon resonance sensors based on waveguide theory," Sci. Rep. **8**, 2560 (2018).
27. C. Zhou, R. Jin, H. He, J. Huang, G. Li, and L. Huang, "Robust ultrahigh-Q resonances in tetramer metasurfaces through centroid symmetry protection and area conservation," Light: Sci. Appl. **15**, 84 (2026).
28. C. Zhou, M. Zhou, Z. Fu, H. He, Z. L. Deng, H. Xiang, X. Chen, W. Lu, G. Li, and D. Han, "Ultrahigh-Q quasi-BICs via precision-controlled asymmetry in dielectric metasurfaces," Nano Lett. **25**, 5916–5924 (2025).
29. M. Kang, L. Mao, S. Zhang, M. Xiao, H. Xu, and C. T. Chan, "Merging bound states in the continuum by harnessing higher-order topological charges," Light: Sci. Appl. **11**, 228 (2022).
30. J. Wang, X. Wang, Z. Wu, X. Zhao, S. Wu, L. Shi, Y. Kivshar, and J. Zi, "Inherent spin-orbit locking in topological lasing via bound state in the continuum," Phys. Rev. Lett. **134**, 133802 (2025).
31. J. Cui, S. Han, B. Zhu, C. Wang, Y. Chua, Q. Wang, L. Li, A. G. Davies, E. H. Linfield, and Q. J. Wang, "Ultracompact multibound-state-assisted flat-band lasers," Nat. Photonics **19**, 643-649 (2025).
32. F. Wu, M. Luo, J. Wu, C. Fan, X. Qi, Y. Jian, D. Liu, S. Xiao, G. Chen, H. Jiang, Y. Sun, and H. Chen, "Dual quasibound states in the continuum in compound grating waveguide structures for large positive and negative Goos-Hänchen shifts with perfect reflection," Phys. Rev. A **104**, 023518 (2021).

AIP Publishing Applied Physics Reviews ACCEPTED MANUSCRIPT
This is the author's peer reviewed, accepted manuscript. However, the online version of record will be different from this version once it has been copyedited and typeset.
PLEASE CITE THIS ARTICLE AS DOI: 10.1063/5.0335616

33. X. Zhang and Y. Wu, "Effective medium theory for anisotropic metamaterials," Sci. Rep. **5**, 7892 (2015).
34. Y. Wu, J. Li, Z. Q. Zhang, and C. T. Chan, "Effective medium theory for magnetodielectric composites: Beyond the long-wavelength limit," Phys. Rev. B **74**, 085111 (2006).
35. B. Zhen, C. W. Hsu, L. Lu, A. D. Stone, and M. Soljacic, "Topological nature of optical bound states in the continuum," Phys. Rev. Lett. **113**, 257401 (2014).
36. Y. Liang, C. Peng, K. Sakai, S. Iwahashi, and S. Noda, "Three-dimensional coupled-wave model for square-lattice photonic crystal lasers with transverse electric polarization: A general approach," Phys. Rev. B **84**, 195119 (2011).
37. Y. Yang, C. Peng, Y. Liang, Z. Li, and S. Noda, "Analytical perspective for bound states in the continuum in photonic crystal slabs," Phys. Rev. Lett. **113**, 037401 (2014).
38. C. W. Hsu, B. Zhen, J. Lee, S. L. Chua, S. G. Johnson, J. D. Joannopoulos, and M. Soljačić, "Observation of trapped light within the radiation continuum," Nature **499**, 188–191 (2013).
39. M. Wan, J. Wang, D. Bao, F. Fan, H. Gao, Z. Qu, and T. Cui, "Terahertz GaAs indicator chip based on high-Q-factor spoof localized surface plasmons resonator," Laser & Photonics Rev. **19**, 2401749 (2025).
40. J. Xie, X. Zhu, X. Zang, Q. Cheng, L. Chen, and Y. Zhu, "Terahertz integrated device: High-Q silicon dielectric resonators," Opt. Mater. Express **8**, 50-58 (2018).
41. S. Romano, M. Mangini, E. Penzo, S. Cabrini, A. C. De Luca, I. Rendina, V. Mocella, and G. Zito, "Ultrasensitive surface refractive index imaging based on quasi-bound states in the continuum," ACS Nano **14**, 15417–15427 (2020).
42. S. Romano, G. Zito, S. Torino, G. Calafiore, E. Penzo, G. Coppola, S. Cabrini, I. Rendina, and V. Mocella, "Label-free sensing of ultralow-weight molecules with all-dielectric metasurfaces supporting bound states in the continuum," Photonics Res. **6**, 726–733 (2018).
43. B. Li, S. Liu, W. Li, Z.-D. Hu, Y. Zhu, J. Wang, Y. Yang, and X. Shen, "Experimental demonstration of merging quasi-BICs in photonic crystal slabs," Mater. & Design **245**, 113263 (2024).
44. Y. Liu, W. Zhou, and Y. Sun, "Optical refractive index sensing based on high-Q bound states in the continuum in free-space coupled photonic crystal slabs," Sensors **17**, 1861 (2017).
45. H. Yan, W. H. Fan, X. Q. Jiang, X. Chen, C. Qin, and Q. Wu, "Dielectric terahertz metasurface governed by symmetry-protected BIC for ultrasensitive sensing," Phys. Scr. **99**, 085503 (2024).
46. A. Ospanova, M. Bukharin, G. Dassano, L. Matekovits, and A. Basharin, "Metamaterial induced bound state in continuum via the self-complementary Babinet principle," Opt. Lett. **50**, 2691-2694 (2025).
47. B. Liu, Y. Peng, Z. Jin, X. Wu, H. Gu, D. Wei, Y. Zhu, and S. Zhuang, "Terahertz ultrasensitive biosensor based on wide-area and intense light-matter interaction supported by QBIC," Chem. Eng. J. **462**, 142347 (2023).